Numerical simulation of mechanical tests on a living skin using anisotropic hyperelastic law

Wael Alliliche, Christine Renaud, Jean-Michel Cros, Zhi-Qiang Feng

Version of Record: https://www.sciencedirect.com/science/article/pii/S175161612300108X
Manuscript_7efdf500bec28c9621d5f373e822d1a3

Numerical simulation of mechanical tests on a living skin using anisotropic hyperelastic law

Wael ALLILICHE[a], Christine RENAUD[a,*], Jean-Michel CROS[a], Zhi-Qiang FENG[a]

[a] *Universite Paris-Saclay, Univ Evry, LMEE, 91020, Evry, France*

Abstract

The skin is a living tissue that behaves in a hyperelastic and anisotropic way. A constitutive law called HGO-Yeoh is proposed to model the skin by improving the classical HGO constitutive law. This model is implemented in a finite element code FER "Finite Element Research" to benefit from its tools, including the bipotential contact method, a very efficient function coupling contact and friction. Identifying the skin-related material parameters is done through an optimisation procedure using analytic and experimental data. A tensile test is simulated using the codes FER and ANSYS. Then, the results are compared with the experimental data. Finally, a simulation of an indentation test using a bipotential contact law is done.

Keywords: Bio-mechanics, contact, nonlinear mechanics, anisotropic hyperelasticity, finite element, skin.

1. Introduction

The skin is the organ that covers the human body to maintain equilibrium; the ability to predict human skin behaviour and evaluate changes in the mechanical properties of the tissue would inform engineering design. It would prove valuable in various disciplines: medical research, prosthesis design or 3D modelling for movies and video games. The aim of our study is to develop a simulation tool including methods not yet found in commercial codes, such as new behaviour laws and other contact methods to simulate indentation and quasi-static suction. This will evolve into dynamics. It is necessary to know the skin's anatomy and structure to model its behaviour. The skin comprises three main layers (Fig. 1).

Epidermis: it represents the outer layer of the skin. Its thickness varies between 0.05 and 1.5 mm [1], depending on the body's part. The epidermis consists of four to five layers of cells called strata.

Dermis: This is the essential layer of the skin. It has a thickness between 0.6 and 4 mm. The dermis is mainly composed of collagen and elastin fibres. These fibres' proportion is more important than the primary material called matrix [2]. Collagen is a protein that structures the skin of mammals. The primary function of collagen is to provide structure and rigidity to the skin. Collagen fibres allow the skin to resist traction [3]. Elastin fibres are perpendicular to collagen ones and essential to maintain skin elasticity. The fundamental substance is a hydrophobic, fat-like gel, representing about 20 % [4] of the skin's total volume, and it is in this substance that the fibres described above are arranged.

Hypo-dermis: its thickness can go up to 30 mm in abdominal skin, as it can be absent in some zones. It is composed mainly of fat cells. This part is not considered in modelling because it does not act on the skin's resistance.

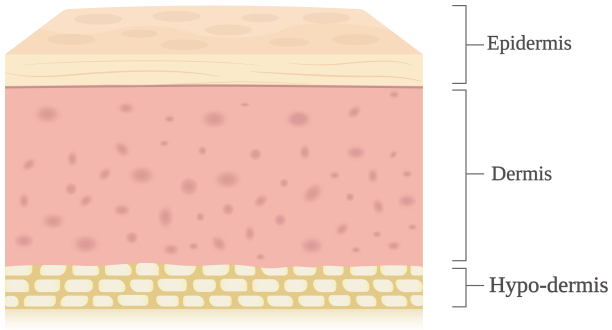

Figure 1: Skin anatomy

The skin behaves like a hyperelastic and almost incompressible material because it is mainly made of water [5]. The dermis contains collagen fibres that make the bio-material anisotropic.

The literature [6] suggests that the viscoelastic behavior of a biological material is mainly due to the interaction between the relatively stiff fibers and the viscous matrix , which allows the material to combine stiffness, flexibility, and shock absorption.

An uniaxial tensile test experimental data are recovered from the literature [7]. Soft tissues are often assumed to be viscoelastic. Although this behaviour was neglected in order to simplify the model, it is planned to improve it later by adding the viscous behavior to the hyperelastic one. Moreover, the data on which this study is based do not allow for viscoelastic identification. Before the experimental test, the skin is prepared [8] in order to focus exclusively on the elastic effects and eliminate the viscoelastic ones.

Our research aims to model the skin by developing an en-

*Corresponding author
Email address: christine.renaud@univ-evry.fr (Christine RENAUD)

ergy density law; it is used for implementation in the finite element code FER [9]. Many constitutive models are used to model skin and soft tissues in literature. Some are only able to model isotropic behaviours, such as the neo-Hookean model [10], Mooney-Rivlin model [11], Ogden model [12], 8-chain model [13], Gent model [14]. The main difference between these models is the trend of the stress-strain curve. Other laws describe both isotropic and anisotropic behaviour of the material, like the HGO model [15].

This paper presents a new strain energy density by coupling the isotropic Yeoh model with the anisotropic HGO model. Next, the bipotential method is proposed to model the contact between the indenter and the skin. After, the identification of our model parameters related to the skin is explained. Finally, the results of a tensile test simulation on FER and ANSYS are compared, and several 3D indentation simulations on the skin are performed. The angle direction of the dominant fibre family is changed at each step, and the anisotropic influence on skin behaviour is analysed.

2. Skin model analysis

2.1. Used invariants

For soft tissue in bio-mechanics, the materials are nonlinear, hyperelastic, and almost incompressible. To take into account the anisotropic of the material, a single direction (**a**) of fibres is chosen. The model assumes that the mean direction of collagen fibres remains aligned with the plane. Indeed, histological examination of the skin [16] indicates that the majority of collagen fibres in the dermis are parallel to the epidermis. The displacement between fibre and matrix plays a negligible role in the elastic behaviour of the skin, since we consider only the main direction of the fibres network. The results obtained from identification in section 3, indicate that the fact of neglecting the displacement between fibre and matrix has no influence. The fibres orientation components are:

$$\mathbf{a} = \{\cos(\alpha), 0, \sin(\alpha)\}, \tag{1}$$

where α is the angle between the collagen fibres and the longitudinal axis of the skin $\vec{x}$ (Fig. 2); This angle is referred to as the local reference frame of elements $(\vec{x}, \vec{y}, \vec{z})_{\text{local}}$. **M** is the orientation matrix of the fibres. α is the angle between the collagen fibres and the longitudinal axis of the skin $\vec{x}$ (Fig. 2). We note **M** as the orientation matrix of the fibres.

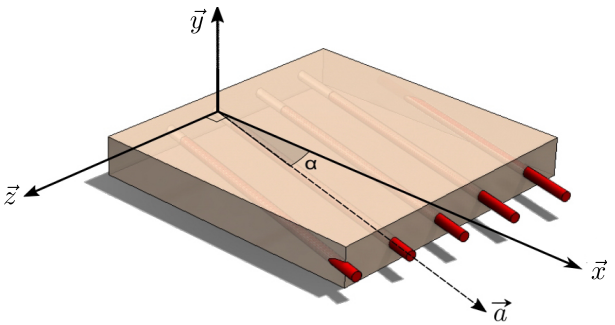

Figure 2: Direction of the fibres $\vec{a}$ according to the angle α

$$\mathbf{M} = (\mathbf{a} \otimes \mathbf{a}). \tag{2}$$

The transformation tensor **F**, the Cauchy-Green strain **C** and the Green-Lagrange strain tensor **E** are defined as:

$$\mathbf{F} = \mathbf{I} + \frac{\partial \mathbf{u}}{\partial \mathbf{X}}, \tag{3}$$

$$\mathbf{C} = \mathbf{F}^T \mathbf{F}, \tag{4}$$

$$\mathbf{E} = \frac{1}{2}(\mathbf{C} - \mathbf{I}), \tag{5}$$

where **u** is the displacement vector and **I** is the identity matrix. Invariants I_1, I_3, I_4 and J are defined by:

$$I_1 = \text{Tr}(\mathbf{C}), \tag{6}$$

$$I_3 = \det(\mathbf{C}), \tag{7}$$

$$I_4 = \text{Tr}(\mathbf{C}\,\mathbf{M}), \tag{8}$$

$$J = \det(\mathbf{F}) = I_3^{\frac{1}{2}}. \tag{9}$$

J represents compression constraint and for isochoric deformation $J \approx 1$ [17]. Isochoric invariants of I_1 and I_4 are used in our model to consider compression variation by introducing I_3 :

$$\bar{I}_1 = I_1 I_3^{-\frac{1}{3}}, \tag{10}$$

$$\bar{I}_4 = I_4 I_3^{-\frac{1}{3}}. \tag{11}$$

2.2. HGO-Yeoh model

The anisotropy of the dermis is due to the collagen fibres, and the isotropy is due to the matrix. So, the behaviour law W is a sum of three deformation energies: isotropic W_{iso}, anisotropic W_{aniso} and volumetric W_{v}.

$$W = W_{\text{iso}} + W_{\text{aniso}} + W_{\text{v}}. \tag{12}$$

To build the model, starting from the HGO model, whose isotropic part is the neo-Hookean model [$W_{iso} = a(I_1 - 3)$]. This part is replaced by the Yeoh model [$W_{iso} = a_i(I_1 - 3)^i$]. The HGO-Yeoh law contains two more parameters and a 3-order polynomial of I_1, which helps to have, as well, a good fitting as a better physical representation. This modification allows obtaining relevant results during the identification. The anisotropic term W_{aniso} [18] is composed of an exponential part that describes the effect of the fibres according to their orientation. Since the materials are nearly incompressible, the third term W_{v} describes compression behaviour. Each term of the equation (12) is given by:

$$W_{\text{iso}}(\bar{I}_1) = \sum_{i=1}^{3} a_i(\bar{I}_1 - 3)^i, \tag{13}$$

$$W_{\text{aniso}}(\bar{I}_4) = \frac{c_1}{2\,c_2}(e^{c_2(\bar{I}_4 - 1)^2} - 1), \tag{14}$$

$$W_{\text{v}}(J) = \frac{1}{d}(J - 1)^2. \tag{15}$$

The constants a_1, a_2, a_3, c_1, c_2 are the material parameters to be defined, d is an expansion parameter that is chosen very small ($d = 10^{-6}$) in incompressible cases, it models the hydrostatic pressure numerically.

In our constitutive model, the fibres only work in tensile. Therefore, there is no effect on the compression, so the part W_{aniso} is under these conditions:

$$\begin{cases} \text{if } I_4 < 1 \; W_{\text{aniso}}(\bar{I}_4) = 0 & \textit{Compression} \\ \text{if } I_4 \geq 1 \; W_{\text{aniso}}(\bar{I}_4) = \dfrac{c_1}{2\,c_2}(e^{c_2\,(\bar{I}_4-1)^2}-1) & \textit{Tensile} \end{cases} \tag{16}$$

2.3. Constraint calculation and implementation

In order to implement this model, the second Piola-Kirchhoff stress tensor $\mathbf{S}$ (17) is defined by derivating the potential W with respect to the strain tensor [19]:

$$\mathbf{S} = \frac{\partial W}{\partial \mathbf{E}} = 2\frac{\partial W}{\partial \mathbf{C}}. \tag{17}$$

Then the calculus by using the partial derivative of $\mathbf{S}$ (17) is developed:

$$\mathbf{S} = 2\frac{\partial W}{\partial \mathbf{C}} \tag{18}$$

$$= 2\left(\frac{\partial W}{\partial I_1}\frac{\partial I_1}{\partial \mathbf{C}} + \frac{\partial W}{\partial I_3}\frac{\partial I_3}{\partial \mathbf{C}} + \frac{\partial W}{\partial I_4}\frac{\partial I_4}{\partial \mathbf{C}} + \frac{\partial W}{\partial J}\frac{\partial J}{\partial \mathbf{C}}\right). \tag{19}$$

This formula of Piola-Kirchhoff constraints is developed by injecting the partial derivatives of W (13) as well as the derivative of the invariants (9) into $\mathbf{S}$ (17):

$$\mathbf{S} = 2\left(\frac{\partial W}{\partial I_1}\mathbf{I} + \frac{\partial W}{\partial I_3}\text{Coef}(\mathbf{C}) + \frac{\partial W}{\partial I_4}\mathbf{M} + \frac{\partial W}{\partial J}\frac{1}{2}\,J\,\mathbf{C}^{-T}\right). \tag{20}$$

Then, the Cauchy stress tensor $\boldsymbol{\sigma}$ is deduced from $\mathbf{S}$ (17) and transformation tensor $\mathbf{F}$ (3):

$$\boldsymbol{\sigma} = \frac{1}{J}\,\mathbf{F}\,\mathbf{S}\,\mathbf{F}^T. \tag{21}$$

2.4. Bipotential contact law

The contact law comes from the bipotential formulation to simulate a skin indentation problem in our finite element code. This law considers two potentials, one associated with Signorini's conditions and the other with Coulomb's law simultaneously. These are coupled in a single non-differentiated potential called bipotential, which means that this method combines contact and friction [20]. This method is implemented in FER, which allows us to simulate indentation. The effectivity of this contact model compared to classical methods has already been demonstrated [21], because it considers the coupling of the normal force and the tangential force in the same formulation of the contact laws and does not use the penalty term that induces interpenetration. The bipotential method translates the complete law of contact with friction into a complementarity constraint. Figure 3 represents the contact reaction $\mathbf{r}$ and its components

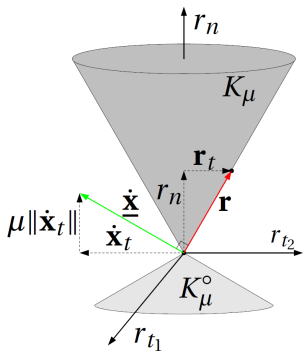

Figure 3: Coulomb's cone representation, special configuration

$(\mathbf{r}_t, r_n)$ as well as the tangential relative velocity $\underline{\dot{\mathbf{x}}}$. The complementary relation, in the general case, is written as follows:

$$\underline{\dot{\mathbf{x}}} = \dot{\mathbf{x}}_t + (\dot{x}_n + \mu\|\dot{\mathbf{x}}_t\|)\,\mathbf{n}. \tag{22}$$

K_μ represents the interior and the edge of the Coulomb cone (Fig. 3), so:

$$b_c(-\dot{\mathbf{x}}, \mathbf{r}) = \begin{cases} \mu\,\|-\dot{\mathbf{x}}_t\|\,r_n & \text{if } \dot{x}_n \geq 0 \text{ and } \mathbf{r} \in K_\mu \\ \text{tend towards } +\infty & \text{otherwise} \end{cases} \tag{23}$$

b_c is a bipotential function interpreted as the dissipated power.

The minus sign preceding the relative tangential velocity emphasises its opposite direction to the frictional force. According to the Implicit Standard Material theory proposed by De Saxcé and Feng [20], the complete law of contact with friction is in the form of a variational inequality. For the numerical solution, our function is adapted to the augmented Lagrangian method, which leads to the following implicit problem:

$$\begin{cases} \text{find} \quad \mathbf{r} \in K_\mu \quad \text{such as} \\ \forall \mathbf{r}' \in K_\mu; \\ (\mathbf{r} - (\mathbf{r} - \varrho(\dot{\mathbf{x}}_t + (\dot{x}_n + \mu\|-\dot{\mathbf{x}}_t\|)\,\mathbf{n}))) \cdot (\mathbf{r}' - \mathbf{r}) \geq 0. \end{cases} \tag{24}$$

with $\varrho > 0$, a parameter whose value ensures a good convergence.

However, $\mathbf{r} \in K_\mu$ must be found in such a way

$$\forall \mathbf{r}' \in K_\mu, \quad (\mathbf{r} - \boldsymbol{\tau}) \cdot (\mathbf{r} - \mathbf{r}') \geq 0, \tag{25}$$

where $\boldsymbol{\tau}$, the contact reaction is given :

$$\boldsymbol{\tau} = \mathbf{r} - \varrho(\dot{\mathbf{x}}_t + (\dot{x}_n + \mu\|-\dot{\mathbf{x}}_t\|)\,\mathbf{n}). \tag{26}$$

$\mathbf{r}$ is the projection of $\boldsymbol{\tau}$ on the Coulomb cone.

The projection ($\mathbf{r} = \text{Proj}_{K_\mu}(\boldsymbol{\tau})$) can be determined analytically, which is why this method is preferred. The expressions of the projection can only correspond to three possible contact statuses: contact with adhesion, contact with sliding and no con-

tact.

$$
\begin{aligned}
&\text{if } \mu\,\|\boldsymbol{\tau_t}^{k+1}\| < -\tau_n^{k+1} \quad \text{then} \qquad \text{(no contact)}\\
&\ \mathrm{Proj}_{K_\mu}(\boldsymbol{\tau}^{k+1}) = 0\\
&\text{else if } \|\boldsymbol{\tau_t}^{k+1}\| < \mu\,\tau_n^{k+1} \quad \text{then} \qquad \text{(adhesion)}\\
&\ \mathrm{Proj}_{K_\mu}(\boldsymbol{\tau}^{k+1}) = \boldsymbol{\tau}^{k+1}\\
&\text{else} \qquad\qquad\qquad\qquad\qquad\qquad \text{(sliding)}\\
&\ \mathrm{Proj}_{K_\mu}(\boldsymbol{\tau}^{k+1}) = \boldsymbol{\tau}^{k+1} - \frac{(\|\boldsymbol{\tau}_t^{k+1}\| - \mu\,\tau_n^{k+1})}{(1+\mu^2)}\left(\frac{\boldsymbol{\tau}_t^{k+1}}{\|\boldsymbol{\tau}_t^{k+1}\|} + \mu\,\mathbf{n}\right)
\end{aligned}
\tag{27}
$$

The vector of contact reactions is built in the global reference frame $\mathbf{R}$ from $\mathbf{r}$.

2.5. Finite element implementation

The HGO-Yeoh model is implemented and simulated within the finite element code FER developed by the "Laboratoire de Mécanique et d'Énergétique d'Évry" (LMEE). The nonlinear geometric analysis can be described using the total Lagrangian formulation. This formulation builds the tangent stiffness matrix using the original configuration, which stays constant and facilitates computation [22]. So, this formulation to describe nonlinear behaviours in our code is used. In the finite element method, the Green–Lagrangian $\mathbf{E}$ strain (5) with linear $\mathbf{B}_{\mathrm{L}}$ and nonlinear terms $\mathbf{B}_{\mathrm{NL}}$ depending on nodal displacements [23] is written. Then the incremental form of $\mathbf{E}$ is:

$$\delta\mathbf{E} = (\mathbf{B}_{\mathrm{L}} + \mathbf{B}_{\mathrm{NL}}(\mathbf{u}))\,\delta\mathbf{u}. \tag{28}$$

From (19) and (28) incremental form formulated:

$$\delta\mathbf{S} = \mathbb{D} : \delta\mathbf{E} = \mathbb{D} : (\mathbf{B}_L + \mathbf{B}_{NL}(\mathbf{u}))\,\delta\mathbf{u}. \tag{29}$$

The elasticity tensor $\mathbb{D}$ derives from $\mathbf{S}$ [24]:

$$\mathbb{D} = 2\,\frac{\partial\mathbf{S}}{\partial\mathbf{C}} = 4\,\frac{\partial^2 W}{\partial\mathbf{C}^2} = \frac{\partial^2 W}{\partial\mathbf{E}^2}. \tag{30}$$

From the virtual displacement, the virtual work δW is:

$$\delta W = \int_{V_0} \delta\mathbf{E}^T\,\mathbf{S}\,dV_0 - \delta\mathbf{u}^T\,\mathbf{F}_{\mathrm{ext}} - \delta\mathbf{u}^T\,\mathbf{R} = 0, \tag{31}$$

V_0 represents the initial volume, $\mathbf{F}_{\mathrm{ext}}$ are the external forces and $\mathbf{R}$ is the vector of contact reactions which are previously resolved.

Since the arbitrary virtual displacement $\delta\mathbf{u}$ can be suppressed, the static equation is :

$$\mathbf{F}_{\mathrm{int}} - \mathbf{F}_{\mathrm{ext}} - \mathbf{R} = 0, \tag{32}$$

where internal forces are given by:

$$\mathbf{F}_{\mathrm{int}} = \int_{V_0} (\mathbf{B}_L + \mathbf{B}_{NL}(\mathbf{u}))^T\,\mathbf{S}\,dV_0. \tag{33}$$

A Newton–Raphson iterative procedure is applied for nonlinear analysis to resolve this kind of problem [23].

3. Skin parameters identification

In this paragraph, the procedure used to determine the material parameters of the *HGO-Yeoh* model (13, 14, 15) from experimental data is explained.

To achieve this goal, we rely on experimental data ($f^{\exp} = \sigma_{xx}^{\exp}(\varepsilon_{xx})$) from a uni-axial tensile test performed on an abdomen skin sample of 30 mm by 30 mm and 4 mm of thickness [7]. An analytic development of the Cauchy stress is used ($f^{\mathrm{th}} = \sigma_{xx}^{\mathrm{th}}(\varepsilon_{xx})$) using (21):

$$
\begin{aligned}
\sigma_{xx}^{\mathrm{th}} = \frac{2\lambda_{11}^2}{J}\Bigg[&\left(\frac{-I_1\ I_3^{-\frac{1}{3}}\ \lambda_{11}^{-2}}{3} + I_3^{-\frac{1}{3}}\right)\\
&\left(a_1 + 2\,a_2\,(I_1\,I_3^{\frac{1}{3}} - 3) + 3\,a_3(I_1\,I_3^{\frac{1}{3}} - 3)^2\right)\\
&+ c_1\left(\frac{1}{3}\,I_4\,I_3^{-\frac{4}{3}} + I_3^{-\frac{1}{3}}\,\cos^2(\alpha)\right)\\
&\left((I_4\,I_3^{-\frac{1}{3}} - 1)\,e^{c_2(I_4\,I_3^{-\frac{1}{3}}-1)^2}\right)\Bigg].
\end{aligned}
\tag{34}
$$

Invariants, and the elongation along x axis λ_{11}, are all related to ε_{11}. The material constants a_1, a_2, a_3, c_1, c_2 are ordered in a vector as the variables of the function:

$$f^{\mathrm{th}} = \sigma_{xx}^{\mathrm{th}}(a_1, a_2, a_3, c_1, c_2). \tag{35}$$

To obtain these parameters, an optimisation process is applied to find a minimal value of the least square error Φ [25] using the Matlab function "fmincon".

$$\Phi = \sum_{i=1}^{n} (\sigma_{xx}^{\exp}(\varepsilon_i) - \sigma_{xx}^{\mathrm{th}}(\varepsilon_i))^2. \tag{36}$$

Fmincon algorithm

"Find a minimum of a constrained nonlinear multivariable function" (*i.e., fmincon*) is a large or medium-scale algorithm that can find a minimum of a scalar function with or without constraints, with several variables starting at initial values [26].

In the identification of the material parameters, experimental data representing results of a uni-axial tensile on a skin sample, taken from the abdomen of a healthy 45-year-old man, are provided from [7].

The direction of collagen fibres has been chosen parallel to the $\vec{x}$ axis in such a way that the angle $\alpha = 0°$.

After 187 iterations, the optimisation algorithm converges. The minimisation of (36) gives us the material parameters related to the skin on table 1.

3.1. Accuracy of the HGO-Yeoh model

A behaviour law is accurate if it can reliably predict the mechanical properties of the skin from the data collected in the experiments. The results predicted by each model (Yeoh, HGO, and HGO-Yeoh) (Sec. 2.2) are compared to the experimental data to evaluate their accuracy.

Using the procedure described above, the Yeoh and HGO model parameters were respectively identified from the uniaxial tensile experimental data [7]. To obtain a fair comparison, the same parameters are used in the optimisation algorithm: machine, MATLAB Optimtool version, stopping criterion, and number of iterations. The parameter values of the models are shown in the table [1].

The experimental data and the analytic results obtained from the optimisation results are plotted in (Fig. 4). The accuracy of the HGO-Yeoh model can be appreciated here. The algorithm

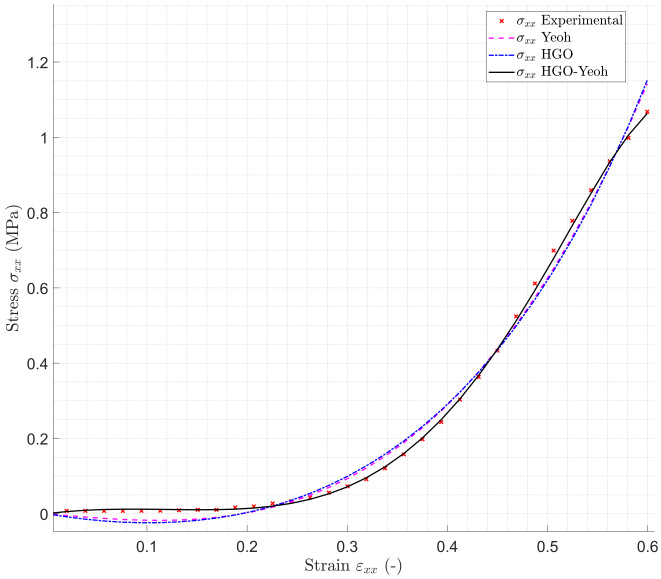

Figure 4: Comparison of experimental results with the hyperelastic laws predictions

computes the relative error between the analytic results and the experimental data for each constitutive law (Fig. 5). The maximum error for the HGO-Yeoh model is less than 2.5 %, while the mean is 0.5 %. The other models have larger errors. The Yeoh model has a mean error of 2.1 %, while the HGO model provides a mean error of 2.5 %. This proves that each law can predict the tensile behaviour, but with a large margin of error. However, when these two constitutive laws are combined, the error is less, and the behaviour prediction is more accurate.

3.2. Parameters sensitivity analysis

Five input parameters characterise our model to give the σ_{xx} output. This model is deterministic, which means that the results obtained are always the same for a given set of input setups (Fig. 6). These input parameters influence the development of the analytic calculation. A sensitivity analysis can determine which parameter has the most influence. This method is generally used for model simplification, to study the robustness of assumptions and to explore the impact of inputs on the output. We set the vector of inputs $\mathbf{P}$, which gathers all the parameters,

$$\mathbf{P} = \begin{pmatrix} \mathrm{P}_1 \\ \mathrm{P}_2 \\ \mathrm{P}_3 \\ \mathrm{P}_4 \\ \mathrm{P}_5 \end{pmatrix} = \begin{pmatrix} a_1 \\ a_2 \\ a_3 \\ c_1 \\ c_2 \end{pmatrix}. \tag{37}$$

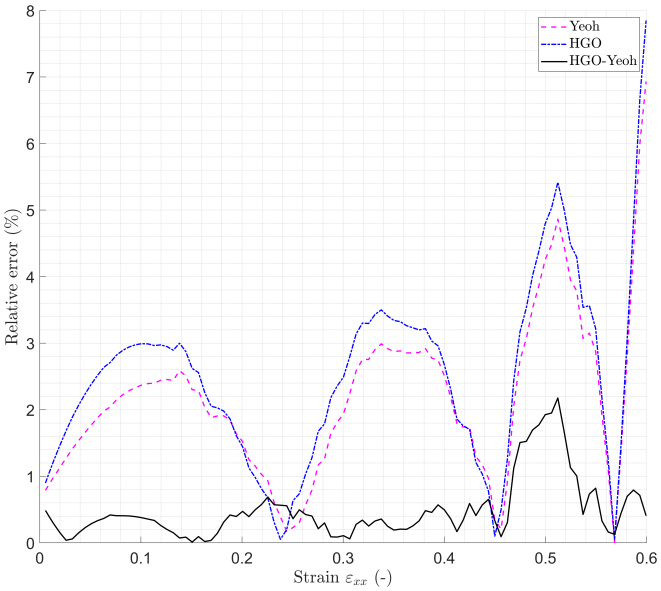

Figure 5: The absolute error between the experimental and the analytical curves

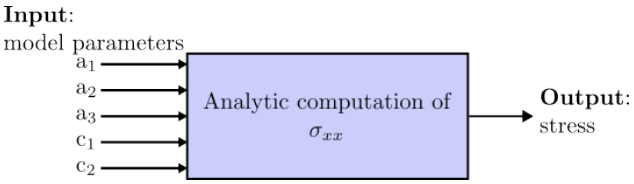

Figure 6: Descriptive schematic of the HGO-Yeoh model

ϕ is the output scalar,

$$\phi(\mathbf{P}) = \sigma_{xx}(\varepsilon_{xx}, \mathbf{P}). \tag{38}$$

The Morris method

This method is often used to calculate the sensitivity of a problem [27]. We have P_j the inputs, where $j = 1, \ldots, 5$; for each j, we construct paths of trajectories in the input space:

$$\mathrm{P}_j^{i+1} = \mathrm{P}_j^i + \Delta_j. \tag{39}$$

With $i = 1, \ldots, n$, we set $n = 1\,000$ for each input parameter. When a parameter is varying, the others are fixed at their values obtained by the identification. Δ_j is the step between two points in the path, and it is set at:

$$\Delta_j = \frac{Ub_j - Lb_j}{n}, \tag{40}$$

Ub_j and Lb_j are the upper and lower bounds used in the identification optimisation for each parameter. P_j^0 is defined at the lower bound Lb_j. Then elementary effect, the gradient of $\phi(\mathbf{P})$ according to parameters, is computed:

$$d_j^i = \frac{\phi(\mathrm{P}_j^{i+1}) - \phi(\mathrm{P}_j^i)}{\Delta_j}. \tag{41}$$

This parameter is calculated for each ε_{xx} point. Then a mean of the elementary effect is calculated over the trajectory path of

Table 1: Identified parameters for hyperelastic models

Parameter	Yeoh	HGO	HGO-Yeoh
a_1 (MPa)	-0.059	0.312	0.269
a_2 (MPa)	0.291	-	0.376
a_3 (MPa)	0.016	-	0.415
c_1 (MPa)	-	-0.297	-0.317
c_2	-	0.087	0.319

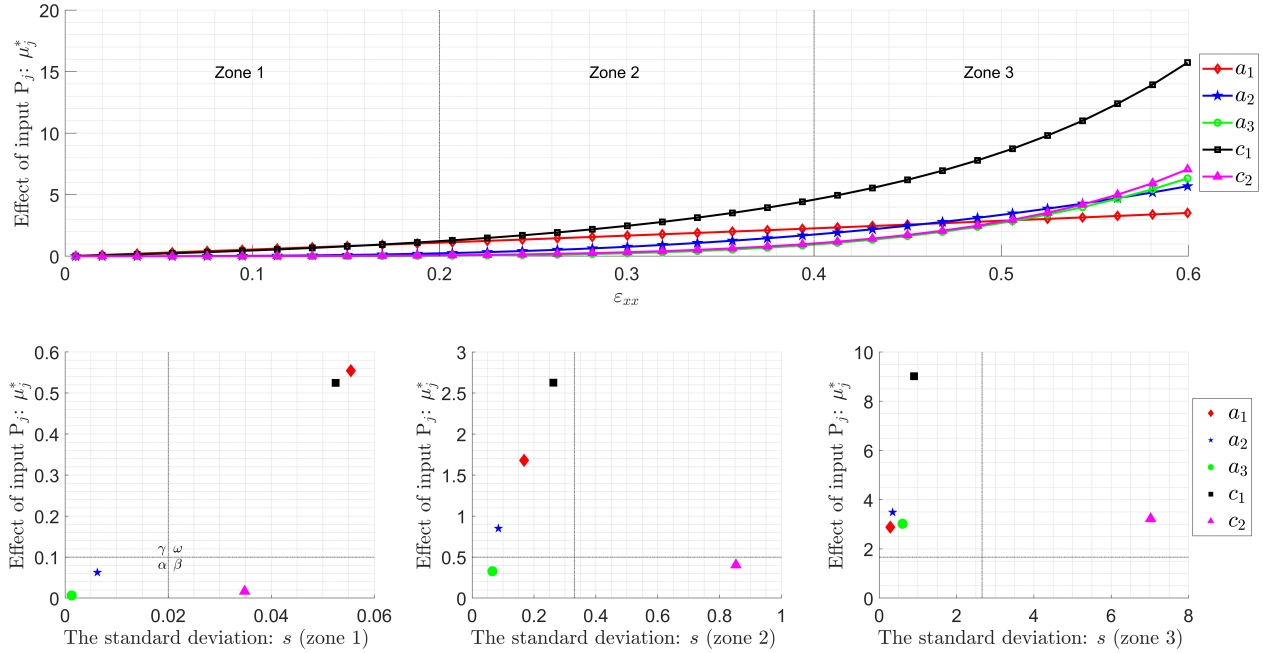

Figure 7: Sensivity analysis of the parameters Effects using Morris Method

inputs. We use the absolute value to avoid the compensation between them:

$$\mu_j^* = \frac{1}{n}\sum_{i=1}^{n}|d_i|. \tag{42}$$

μ_j^* represents the effect of the input P$_j$ on the output $\sigma_{xx}(\varepsilon_{xx}, P_j)$. The 1st graphic on the (Fig. 7) represents the evolution of the effect of each parameter on the model according to strain ε_{xx}.

Finally, the standard deviation (s) is estimated to complete the Morris method:

$$s_j = \sqrt{\frac{1}{n-1}\sum_{i=1}^{n}(d_j^i - \mu_j^*)}. \tag{43}$$

The Morris method gives the sensitivity at a specific local point of ε_{xx}. To have a global vision, we calculate the mean over the strain points of the effects of inputs and the standard deviations. We divided the field of strain into three zones to analyse the influence of parameters in each one:

$$\begin{aligned} &\text{Zone 1}: \quad \text{if} \quad \varepsilon_{xx} \in [0.0, 0.2], \\ &\text{Zone 2}: \quad \text{if} \quad \varepsilon_{xx} \in [0.2, 0.4], \\ &\text{Zone 3}: \quad \text{if} \quad \varepsilon_{xx} \in [0.4, 0.6]. \end{aligned}$$

The different parameters are interpreted according to μ_j^* and s_j:

- for a weak value of μ_j^*, input parameters are neglected.
- for a strong value of μ_j^* and a weak value of s_j, input parameters are important with linear effect.
- for a strong value of μ_j^* and a strong value of s_j, input parameters are important with non-linear effect.

In our case, the effect depends on the zone. For example, the parameter a_1 is always strong but loses its influence on the non-linearity as a function of the strain. The parameter a_3 has a linear effect, and its importance increases along ε_{xx}. However, the parameter c_2 gain strength gains in strength but still affects the nonlinearity.

4. Simulation of mechanical tests on skin

4.1. ANSYS Material configuration

To validate the HGO-Yeoh model implementation, the FER simulation is compared with the ANSYS simulation. We could then build on a correct basis and feed it further with methods that are not available in commercial codes.

ANSYS [28] proposes in addition to the classical laws, a nonlinear hyperelastic anisotropic constitutive law that uses 11 parameters to describe the elastic properties of a material. This

law is not referenced in the textbook bibliography. It is based on 4 isochoric invariants $\bar{I}_1$, $\bar{I}_2$, $\bar{I}_4$ and $\bar{I}_6$:

$$W(\bar{I}_1, \bar{I}_2, \bar{I}_4, \bar{I}_6, J) = \sum_{i=1}^{3} \left(C_i(\bar{I}_1 - 3)^i + C_{(i+3)}(\bar{I}_2 - 3)^i \right) + \frac{C_7}{2C_8}(e^{C_8(\bar{I}_4-1)^2}-1) + \frac{C_9}{2C_{10}}(e^{C_{10}(\bar{I}_6-1)^2}-1) + \frac{1}{d}(J-1)^2 \quad (44)$$

To obtain the HGO-Yeoh hyperelastic anisotropic constitutive law from equation (44), the parameters of the strain energy potential related to the stress invariants $\bar{I}_2$ and $\bar{I}_6$ must be removed. To satisfy this condition $C_4 = C_5 = C_6 = C_9 = 0$ whatever C_{10}.

It is also important to ensure that the other parameters are set appropriately to reproduce the desired elastic properties of the skin. Therefore, the identified parameters of the HGO-Yeoh model (a_1, a_2, a_3, c_1 and c_2), in table 1, are set respectively on the ANSYS material parameters (C_1, C_2, C_3, C_7, and C_8) It is important to keep in mind that altering the parameters of the constitutive law may affect its accuracy for the intended applications. Therefore, comparing the results obtained with experimental data is important to confirm the mechanical properties' validity.

4.2. Uni-axial tensile test

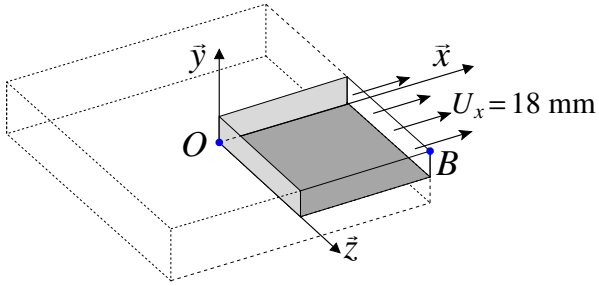

Figure 8: Description of uni-axial tensile test on skin

This part performs a simulation of the experimental trial extracted from [7]. The skin sample is modeled by a brick of dimension (60 mm, 8 mm, 60 mm). Considering the symmetry conditions, only $\frac{1}{8}$ of the shape is meshed with only one 8-node hexahedral element. Indeed, symmetry conditions are applied on the planes $(\vec{y}, \vec{z})$, $(\vec{x}, \vec{z})$, $(\vec{x}, \vec{y})$ where displacements are respectively set at $u_x = 0$, $u_y = 0$, $u_z = 0$ (Fig. 8), and 100 loads of 0.18 mm are applied on the face where $x = 30$ mm, which gives finally a displacement of 18 mm. This simulation is done separately in both FER et ANSYS finite elements codes using the same inputs setting and the same hyperelastic HGO-Yeoh material parameters identified in table 1.

The curves on (Fig. 9) represent σ_{xx}^{FER} and $\sigma_{xx}^{\text{ANSYS}}$, according to the deformation ε_{xx}, the obtained curves with the experimental one are compared. The numerical result curves agree with the experimental ones for both simulations and perfectly coincide with the analytic curves. Figure 10 shows us the stress at different strains and different iterations. Several

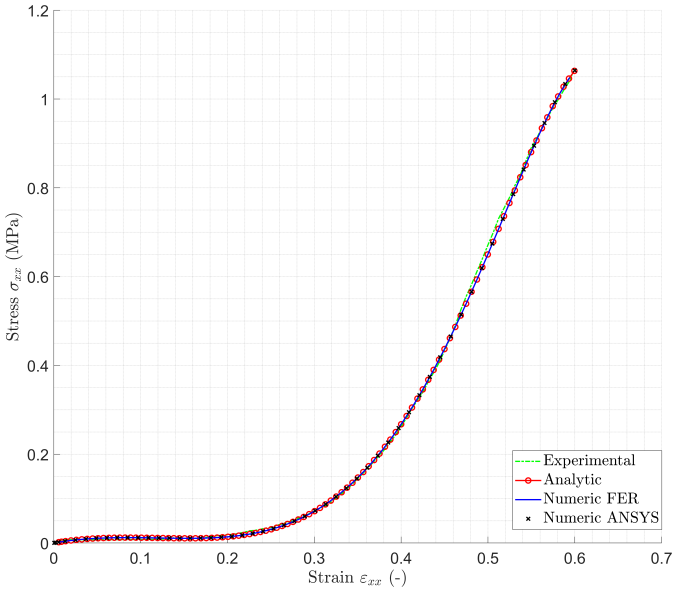

Figure 9: Comparison of experimental results with the FER and ANSYS results

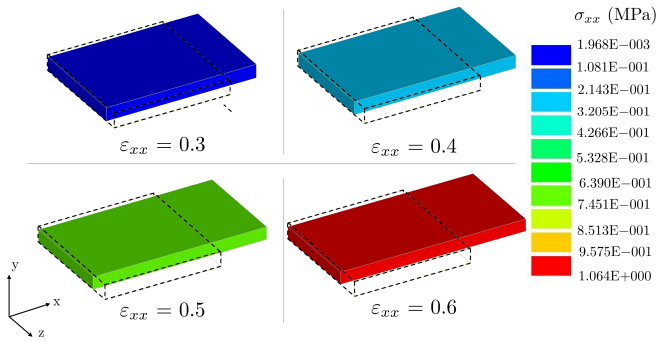

Figure 10: Stress and deformation of the skin under tensile test simulated on FER

simulations are performed at point B (Fig. 8), which position is defined by the vector $\overrightarrow{OB}$ = (30 mm, 4 mm, 30 mm), where O is the origin point. Then a simulation of a compression test using the same displacement according to $-\vec{x}$. The stress is more critical with compression (Fig. 11) because the fibres do not work, so the matrix is more solicited, and the von Mises stresses are higher. However, according to our model, those collagen fibres should only work in tension (16), and in compression, they distort without being stressed like an elastic string. As a displacement is imposed and the coefficient of the anisotropic part c_1 is negative, when the structure is tensile, the fibre works in compression to maintain equilibrium and reduce the stress on the material. Bio-mechanically, this describes the mechanism: when the skin matrix is under tension, the fibres work in compression to reduce the pressure on the skin. So the anisotropic stress is negative, contrary to the constants related to the isotropic terms.

The fibres' orientation angle α is changed at each new tensile test. The results are presented in table [2] below. These values are taken when the strain is maximal. When the fibre

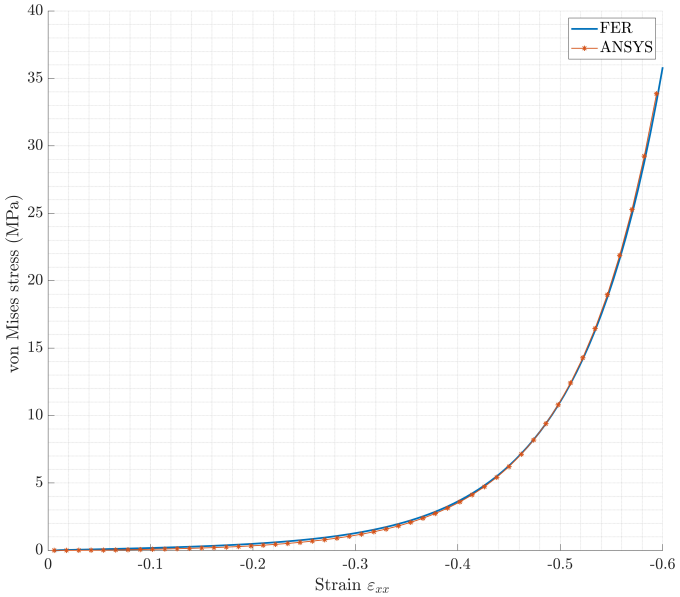

Figure 11: Stress and deformation of the skin in a compression simulation

orientation is different from zero, and in the case of pure tensile stress according to $\vec{x}$, the fibres are in tension according to $\vec{x}$ and in compression according to $\vec{y}$.

Displacement u_x is always equal to 18 mm as it is the imposed loading. In the table [2], the displacements u_y and u_z are almost identical with FER and ANSYS, regardless of the orientation angle of the fibres.

For the 0° orientation, the results on FER and ANSYS are the same as the analytic results, knowing that a numerical zero is obtained concerning the component of the stress σ_{yy}. Indeed, in our case, it is pure traction. The result on FER σ_{yy}^{FER} is closer to zero than the one on σ_{yy}^{ANSYS}, so the modelling on FER is more accurate.

When the orientation of the fibres is at 30°, 45° and 60°, σ_{xx} component along the tensile axis is more significant with the *HGO-Yeoh* model. The σ_{yy} is negative with the *HGO-Yeoh* model since it is positive with the ANSYS model. This phenomenon is studied on [29]. However, a difference on σ_{zz} is observed. The displacement u_z is negative, so it causes à compression according to $\vec{z}$ because, in our model, the fibres work only in tensile. So, the stress is slightly higher in the *HGO-Yeoh* model.

4.3. Indentation test on skin

An indentation of a rigid sphere applied to human skin is simulated. The radius of the sphere is 2.5 mm. The deformable-body is a paralleled-rectangles of dimensions 30 mm × 4 mm × 30 mm in the global reference frame $(\vec{x},\vec{y},\vec{z})_{\text{global}}$. An empty half-sphere models the indenter to reduce the number of elements and, thus, the computational cost. The mesh has 17 980 nodes and is composed of 12 336 8-node hexahedral elements. The material parameters obtained from the identification (Sect. 3) are used. We assume that the abdomen has the same friction properties as the anterior legs. If the indenter is considered as an aluminium sphere, the friction coefficient between the indenter and the skin could be: $\mu_{Al}^{skin} \approx 0.34$ [30].

The displacement of the indenter is applied through 100 steps of $0,01$ mm. Thus, the indenter undergoes a total vertical displacement of 1mm. For the post-processing of the results, the equivalent von Mises stress at point M, the first contact point, and the vertical displacements at points A, B, C, and D are calculated. These four observation points are strategically placed on the axes of symmetry of the deformable body (Fig. 12). Figure 13 represents the evolution of the von Mises stress

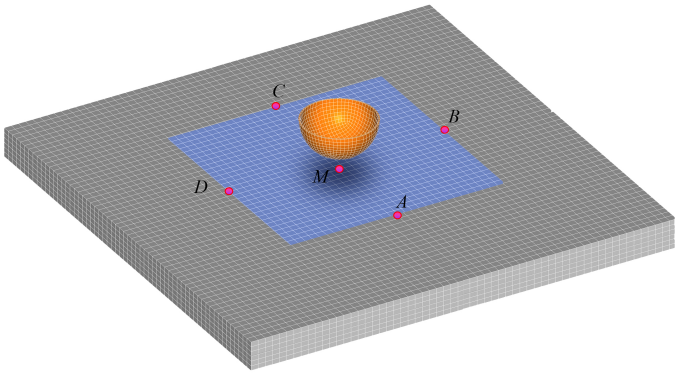

Figure 12: Mesh and observation points

measured at the point M as a function of the displacement of the indenter U_y^{ind}. A typical exponential trend of a hyperelastic material curve is observed. The stress measured at the point M is very low until $U_y^{\text{ind}} = 0.4$ mm. From this value, the equivalent stress evolves exponentially from 4.75 MPa to 311 MPa for $U_y^{\text{ind}} = 1$ mm. Now, the deformation of the skin is analysed. The

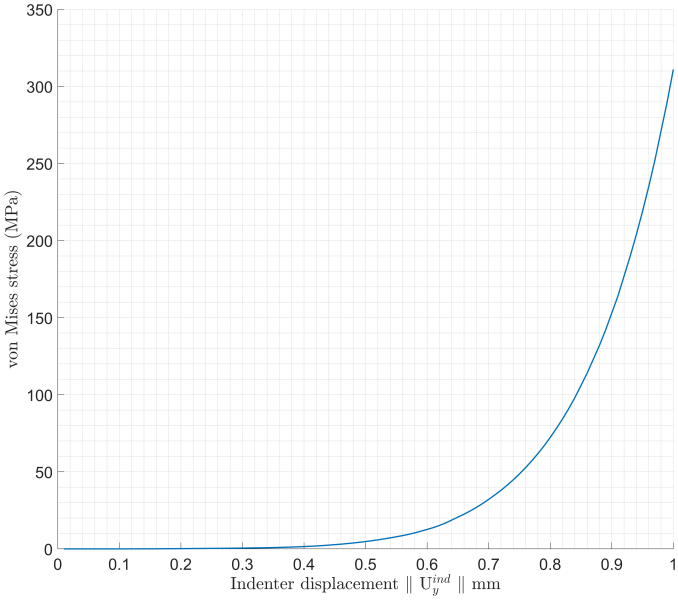

Figure 13: Evolution of von Mises stress as a function of indentor displacement U_y^{ind}

angle α (Fig. 2) is varied between 0° and 180° taking 8 intermediate values. The displacements of the skin U_y^{skin} along the

Table 2: Results of uni-axial traction simulations at different angles with FER and ANSYS on point B

Angle	Code	u_y(mm)	u_z(mm)	σ_{xx}(MPa)	σ_{yy}(MPa)	σ_{zz}(MPa)	σ_{mises}(MPa)
0°	Analytic	−0.860	−6.450	1.064	0	0	1.064
	FER	−0.837	−6.279	1.064	$-3.248e^{-13}$	$3.246e^{-13}$	1.064
	ANSYS	−0.837	−6.282	1.064	$0.379e^{-5}$	$0.379e^{-5}$	1.064
30°	FER	−1.0736	−4.375	4.574	−0.153	0.306	4.613
	ANSYS	−1.029	−3.827	4.433	0.018	0.267	4.367
45°	FER	−0.9703	−5.203	6.077	$-3.82e^{-2}$	0.171	6.030
	ANSYS	−0.945	−5.102	5.979	$0.118e^{-2}$	0.108	5.935
60°	FER	−0.858	−6.075	6.494	$-3.323e^{-4}$	$3.246e^{-2}$	6.480
	ANSYS	−0.857	−6.087	6.321	$0.189e^{-3}$	$0.145e^{-2}$	6.514

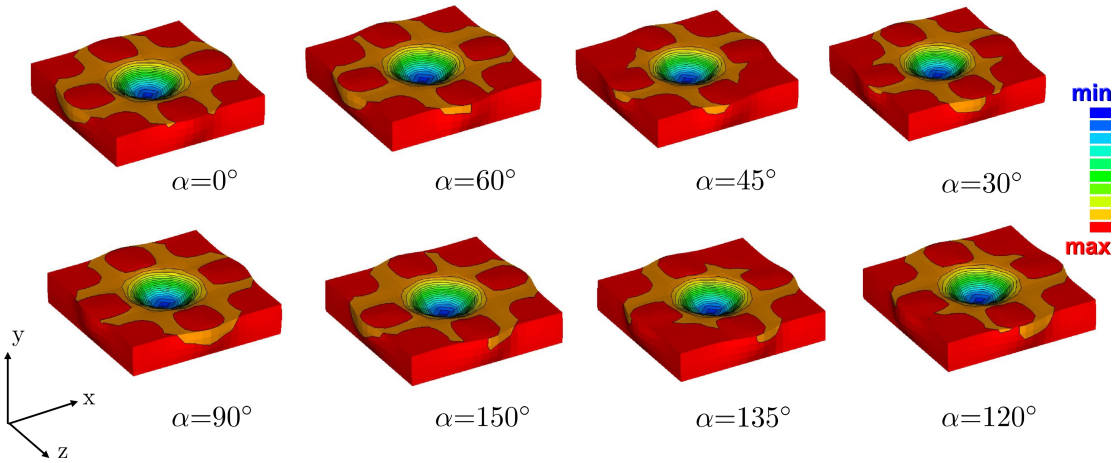

Figure 14: Displacement fields U_y^{skin} according to the angle α

$\vec{y}$ axis are studied. Figure 14 shows the displacement field according to these different angles. The blue colour represents the minimal displacement in negative values, and the red represents the maximal displacement in positive values. The maximum displacement is observed at the periphery of the indentation. These displacements vary according to the α angle. The rest of the study will focus on the non-contact zone.

The deformations change according to the anisotropy. Depression zones at the skin surface appear. These zones, in orange, follow the direction of the fibres. For example, when $\alpha = 0°$, there are more deformations on the $\vec{x}$ axis, and when $\alpha = 90°$, the deformations are more important on the $\vec{z}$ axis. There is also a double symmetry of the displacement distribution for the axes, $\vec{x}$ and $\vec{z}$, for the angles: 60° and 150°, 45° and 135°, 30° and 120°. These symmetries are due to the fibres that prevent the flexible material from deforming in the direction of the axis normal to the $\vec{y}$ plane.

Figure 15 represents these displacements at the 50th increment, where $U_y^{ind} = 0.5$ mm. It shows that the opposite points A and C, B and D, move mutually in the same way as a function of angles. This proves the anisotropy of the model. The minimum value of displacements is observed for angles 30° and 120° at points A and C. The maximum displacement is observed for angles 0 and 180°. For the points B and D, the same observations are made with a phase shift of 90°. The intersection of the four curves occurs for the angle 45° for which the vector of the equation (1) is $\mathbf{a} = \{\frac{\sqrt{2}}{2}, 0, \frac{\sqrt{2}}{2}\}$. To better visualise this phenomenon, the values of the displacements U_y^{skin} of the points A, B, C, D are recorded for each anisotropy angle α. The evolution of the displacement U_y^{skin} as a function of U_y^{ind} of the 4 points is plotted in figure 16. The *HGO-Yeoh* model is used with an angle of 60°. The parameter c_1 is first cancelled to obtain an isotropic behaviour law of *Yeoh*. For the latter, the displacement of the 4 points is identical, unlike the anisotropic material, where the opposite points move two by two: A with C and B with D. During indentation, the hyperelastic materials swell at the borders at the beginning of the operation; then, a subsidence relative to the displacement of the indenter appears. As expected, points A and C show a more pronounced decline than points B and D.

4.4. Influence of the mesh in anisotropic materials

During the modelling process, two different meshes are created. Mesh 1 (Fig. 17) was first made to reduce the number of elements while keeping a refinement of the mesh in the contact zone, the objective being to lower the computation time. The U_x^{skin} displacements distribution obtained with this mesh

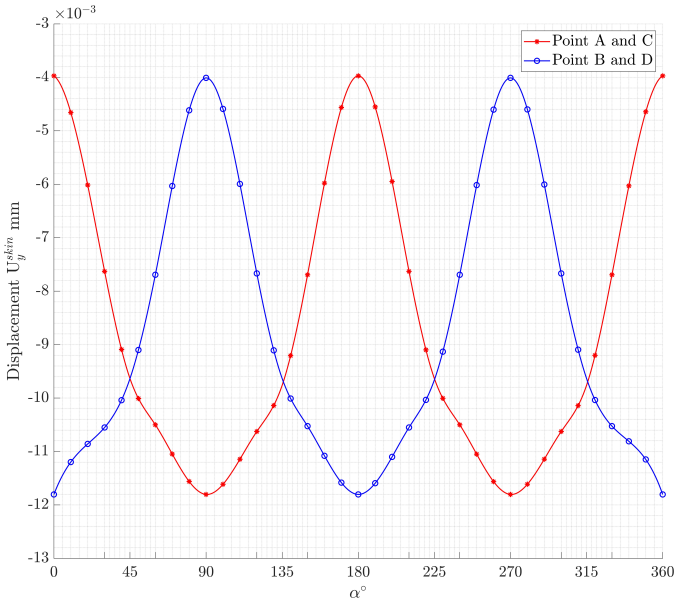

Figure 15: Variation of displacements U_y^{skin} as a function of anisotropy at points A, C and B , D

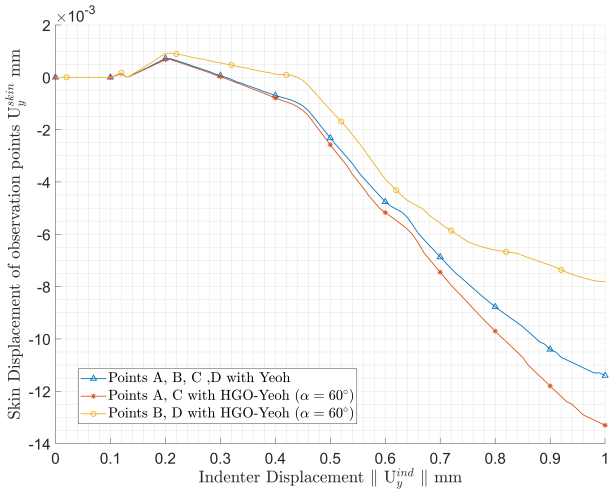

Figure 16: U_y^{skin} displacement of points A, B, C, D according to U_y^{ind} and comparison between *HGO-Yeoh* and Yeoh constitutive laws

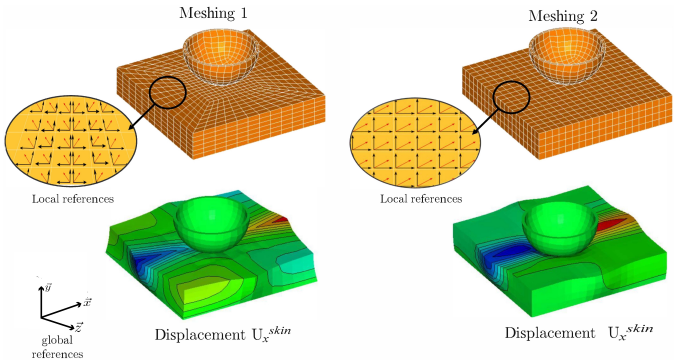

Figure 17: Meshing influence in anisotropic materials

shows sharp angles visible at the location of the four observation points (A, B, C and D on Fig. 12). These angular points disappear when regular hexahedral elements are used, such as in mesh 2. The local reference points of these elements are then oriented like the global reference point, which is not the case in the first mesh. The direction of the fibres for the local reference frame is given, so the reference frame mismatch explains the anomalies observed here. Thus, particular attention should be paid to the mesh used to simulate the behaviour of anisotropic materials.

5. Conclusion

In this work, the identification of the parameters used in the *HGO-Yeoh* model has been successfully realised to simulate mechanical actions on a hyperelastic anisotropic material such as the skin. However, this is only an example of a given sample. In nature, the skin differs between individuals according to age, ethnicity, gender, and health status. Our study aims mainly to show that our model is usable for modelling human skin and explaining the procedure to follow to identify the parameters of this model. To go further, other experimental data from other specimens must be used. However, the identification process of the *HGO-Yeoh* behaviour law from experimental data in a uniaxial tensile test is validated. With this hyperelastic anisotropic model, an indentation test has been simulated. The results are coherent and logical, and no convergence problems are faced. So, a robust model is used, and it will allow us to do more complex contact simulations with the *HGO-Yeoh* law. Nevertheless, our modelling does not take into account the variation of fibres' direction in one simulation. Thus, the anisotropy is the same for all finite elements. This is why only small-scale examples were treated in this paper. Some simplifications are considered, assuming that the skin comprises only one layer. In nature, it is stratified into three layers (epidermis, dermis, hypodermis) material. This simplification is due to the difficulty of carrying out mechanical tests capable of considering these different layers. The variation of the direction of the fibres, giving the skin the property of anisotropy, presents an obstacle in large-scale skin modelling; a thick mesh with different anisotropy directions with a local reference for each element must be used. Future work also concerns the consideration of adhesion with more efficient models than those present in commercial finite element codes. The integration of viscoelastic behaviour to the HGO-Yeoh law is being started to treat more complex dynamic problems .

References

[1] S. Nafisi, H. I. Maibach, Skin penetration of nanoparticles, in: R. Shegokar, E. B. Souto (Eds.), Emerging Nanotechnologies in Immunology, Micro and Nano Technologies, Elsevier, Boston, 2018, Ch. 3, pp. 47–88. doi:https://doi.org/10.1016/B978-0-323-40016-9.00003-8.

[2] G. Limbert, Constitutive Modelling of Skin Mechanics, Springer International Publishing, Cham, 2019. doi:10.1007/978-3-030-13279-8_2.

[3] J. Lin, Y. Shi, Y. Men, X. Wang, J. Ye, C. Zhang, Mechanical roles in formation of oriented collagen fibers, Tissue Engineering Part B: Reviews

26 (2) (2020) 116–128, pMID: 31801418. doi:10.1089/ten.teb.2019.0243.

[4] D. Remache, Contribution à l'étude expérimentale et numérique du comportement hyperélastique et anisotrope de la peau humaine., Theses, Institut FEMTO-ST - Université Franche-Comté (Dec. 2013).
URL https://tel.archives-ouvertes.fr/tel-01117057

[5] F. Xu, T. Lu, Skin Structure and Skin Blood Flow, Springer Berlin Heidelberg, Berlin, Heidelberg, 2011, Ch. 2, pp. 7–19. doi:10.1007/978-3-642-13202-5_2.

[6] H. Ghorbel-Feki, A. Masood, M. Caliez, M. Gratton, J. C. Pittet, M. Lints, S. Dos Santos, Acousto-mechanical behaviour of ex-vivo skin: Nonlinear and viscoelastic properties, Comptes Rendus Mécanique 347 (3) (2019) 218–227. doi:https://doi.org/10.1016/j.crme.2018.12.005.

[7] L. Socci, G. Pennati, F. Gervaso, P. Vena, An axisymmetric computational model of skin expansion and growth, Biomechanics and modeling in mechanobiology 6 (2007) 177–88. doi:10.1007/s10237-006-0047-9.

[8] A. Menzel, Modelling of anisotropic growth in biological tissues, Biomechanics and Modeling in Mechanobiology 3 (3) (2005) 147–171. doi:10.1007/s10237-004-0047-6.

[9] Z.-Q. Feng, B. Magnain, J.-M. Cros, Solution of large deformation impact problems with friction between blatz–ko hyperelastic bodies, International Journal of Engineering Science 44 (1) (2006) 113–126. doi:https://doi.org/10.1016/j.ijengsci.2005.06.006.

[10] M. Mooney, A theory of large elastic deformation, Journal of Applied Physics 11 (9) (1940) 582–592. doi:10.1063/1.1712836.

[11] R. S. Rivlin, Large elastic deformations of isotropic materials iv. further developments of the general theory, Philosophical Transactions of the Royal Society of London. Series A, Mathematical and Physical Sciences 241 (835) (1948) 379–397. doi:10.1098/rsta.1948.0024.

[12] R. W. Ogden, Large deformation isotropic elasticity - on the correlation of theory and experiment for incompressible rubberlike solids, Proceedings of the Royal Society of London. A. Mathematical and Physical Sciences 326 (1567) (1972) 565–584. doi:10.1098/rspa.1972.0026.

[13] E. M. Arruda, M. C. Boyce, A three-dimensional constitutive model for the large stretch behavior of rubber elastic materials, Journal of the Mechanics and Physics of Solids 41 (2) (1993) 389 – 412. doi:https://doi.org/10.1016/0022-5096(93)90013-6.

[14] A. N. Gent, A New Constitutive Relation for Rubber, Rubber Chemistry and Technology 69 (1) (1996) 59–61. doi:10.5254/1.3538357.

[15] G. A. Holzapfel, T. C. Gasser, R. W. Ogden, A new Constitutive Framework for Arterial Wall Mechanics and a Comparative Study of Material Models, Springer Netherlands, Dordrecht, 2001, Ch. 61, pp. 1–48. doi:10.1007/0-306-48389-0_1.

[16] A. Ní Annaidh, K. Bruyère, M. Destrade, M. D. Gilchrist, C. Maurini, M. Otténio, G. Saccomandi, Automated estimation of collagen fibre dispersion in the dermis and its contribution to the anisotropic behaviour of skin, Annals of Biomedical Engineering 40 (8) (2012) 1666–1678. doi:10.1007/s10439-012-0542-3.

[17] R. W. Ogden, Non-linear elastic deformations., ZAMM - Journal of Applied Mathematics and Mechanics / Zeitschrift für Angewandte Mathematik und Mechanik 65 (9) (1984) 404–404.

[18] G. Chagnon, J. Ohayon, J.-L. Martiel, D. Favier, Hyperelasticity modeling for incompressible passive biological tissues, in: Biomechanics of Living Organs, Vol. 1 of Translational Epigenetics, Academic Press, Oxford, 2017, pp. 3–30. doi:https://doi.org/10.1016/B978-0-12-804009-6.00001-8.

[19] F. Peyraut, C. Renaud, N. Labed, Z.-Q. Feng, Modélisation de tissus biologiques en hyperélasticité anisotrope – Étude théorique et approche éléments finis, Comptes Rendus Mécanique 337 (2) (2009) 101 – 106. doi:https://doi.org/10.1016/j.crme.2009.03.007.

[20] G. De Saxcé, Z.-Q. Feng, The bipotential method: A constructive approach to design the complete contact law with friction and improved numerical algorithms, Mathematical and Computer Modelling 28 (4) (1998) 225 – 245, recent Advances in Contact Mechanics. doi:https://doi.org/10.1016/S0895-7177(98)00119-8.

[21] C. Renaud, J.-M. Cros, Z.-Q. Feng, B. Yang, The yeoh model applied to the modeling of large deformation contact/impact problems, International Journal of Impact Engineering 36 (5) (2009) 659–666. doi:https://doi.org/10.1016/j.ijimpeng.2008.09.008.
URL https://www.sciencedirect.com/science/article/pii/S0734743X08002352

[22] M. A. Crisfield, Nonlinear finite element analysis of solids and structures. Volume 1: Essentials, Wiley Professional Software, 1991.

[23] J. Simo, T. Hughes, Computational Inelasticity, Springer-Verlag New York, 1998. doi:https://doi.org/10.1007/b98904.

[24] J. Schröder, P. Neff, D. Balzani, A variational approach for materially stable anisotropic hyperelasticity, International Journal of Solids and Structures 42 (15) (2005) 4352 – 4371. doi:https://doi.org/10.1016/j.ijsolstr.2004.11.021.

[25] D. W. Marquardt, An algorithm for least-squares estimation of nonlinear parameters, Journal of the Society for Industrial and Applied Mathematics 11 (2) (1963) 431–441.

[26] A. Meddour, N. Rizoug, A. Babin, L. Degaa, Optimization of Li-ion modelling for automotive application: comparison of optimization methods performances, in: 2020 7th International Conference on Control, Decision and Information Technologies (CoDIT), Vol. 1, 2020, pp. 1117–1122. doi:10.1109/CoDIT49905.2020.9263841.

[27] J. Morio, Global and local sensitivity analysis methods for a physical system, European Journal of Physics 32 (6) (2011) 1577–1583. doi:10.1088/0143-0807/32/6/011.

[28] ANSYS®, Theory Reference, Ansys Inc., 2022.

[29] Z.-W. Chen, P. Joli, Z.-Q. Feng, Anisotropic hyperelastic behavior of soft biological tissues, Computer Methods in Biomechanics and Biomedical Engineering 18 (13) (2015) 1436–1444. doi:https://doi.org/10.1080/10255842.2014.915082.

[30] M. Zhang, A. F. T. Mak, In vivo friction properties of human skin, Prosthetics and Orthotics International 23 (2) (1999) 135–141, pMID: 10493141. doi:10.3109/03093649909071625.